Thermal Design of Detector for the Solar X-Ray and Extreme Ultraviolet Imager

Shijun Li,* Liheng Chen,† and Yuhua Wu‡
Chinese Academy of Sciences, Changchun, Jilin 130033, People's Republic of China

DOI: 10.2514/1.T5423

The thermal design of detector in a solar X-ray and extreme ultraviolet imager is performed according to the specific requirements for the temperature of its optical system. First, the detector structure and the thermal control index are introduced. Second, the external heat fluxes of the imager is analyzed, and the position of the heat dissipation surface is confirmed. Then, the factors that influence the temperature of the charge-coupled device are analyzed. Large-thermal-resistance insulating technology is adopted, and a detailed thermal design scheme is proposed based on the difficulty of the thermal design. A thermal analysis model is constructed using thermal model generator software. Finally, a thermal balance test is performed in a vacuum environment. Simulation results show that the temperature of the charge-coupled device ranges from −69.7 to −61.3°C, which meets the thermal control index requirements. Test results indicate that the charge-coupled device temperature range from −69.3 to −62.2°C, which also satisfies the design requirements. Additionally, the test values are in good agreement with the calculated results, which verify that the thermal design is appropriate.

Nomenclature

α_s = solar absorptivity
ε = emissivity

I. Introduction

WHEN violent activity breaks out in the sun, large amounts of materials (including magnetic fields, high-energy particles, and high-energy electromagnetic waves) are projected into the interplanetary space over a very short period of time. This will cause major disturbances in the near-Earth space environment and can lead to poor weather. Occasionally, this activity may have catastrophic consequences that result in huge economic losses [1]. Solar activity phenomena in the corona and the chromosphere are intense, with radiation that is mainly concentrated in the extreme ultraviolet (EUV) and X-ray bands [2]. The radiation of X rays reflects the processes of change in the high-temperature plasma of the corona. The effects of the 19.5 nm EUV spectrum on the observation of certain solar activities or phenomena that are accompanied by outbreaks of activity in the sun are very good and can make up for a lack of X-ray observations. Therefore, instruments for observation of the sun are generally focused on operation in the X-ray and EUV bands.

Space-based observation of the sun began in 1960, and the Pioneer 5 spacecraft from the United States was the first ship to observe the sun [3]. On 2 December 1995, the Solar and Heliospheric Observatory (SOHO) was launched by NASA, and 12 major scientific instruments were installed on the SOHO [4]. Each of these instruments could observe part of the sun or the entire sun independently. The Solar-B spacecraft developed by Japan, the United Kingdom, and the United States was launched on 22 September 2006, with the main purpose of observing the fine structure of the sun's magnetic field and studying the intense activities involved in the outbreaks of solar flares [5–7]. The Solar-B carried three instruments with very complex internal structures. Additionally, the temperature of the charge-coupled device detector for operation in the X-ray and visible light bands was required to be cooled down to less than −43°C, and the charge-coupled device (CCD) could move along the Z direction by ±1 mm. Solar Orbiter will be launched by the European Space Agency (ESA) in 2018. ESA's Solar Orbiter mission is conceived to perform a close-up study of our sun and inner heliosphere (the uncharted innermost regions of our solar system), and even predict the unruly behavior of the star on which our lives depend. At its closest point, the spacecraft will be closer to the sun than any previous spacecraft, braving the fierce heat, and will carry its telescopes to almost one-quarter of Earth's distance from our nearest star [8–10]. It will provide unique data and imagery of the sun. At present, the solar X-ray and EUV imager (XEUVI) from the People's Republic of China is being studied as the latest international equipment for the monitoring of solar activity. The equipment integrates the imaging functions of the X-ray band and the 19.5 nm EUV spectrum to capture more of the sun's outburst phenomena or other associated phenomena. With high photon energy and with the refractive index in all materials being close to one, grazing incidence focusing can only be adopted for imaging in the X-ray band [11]. However, positive incidence focusing can be used for imaging in the EUV band. The same set of image sensors is used in two bands. An integrated imager design for both the positive incidence and grazing incidence was first proposed internationally and has been successfully designed in China. The instrument is mounted on the FY-3 meteorological satellite for the first time, and successful operation of the instrument in orbit will greatly improve the satellite's ability to monitor and forecast space weather.

The detector that is studied in this paper is installed on the XEUVI. The temperature of the CCD is required to be controlled within the −75 to −55°C range, which represents a large temperature difference with the temperature of the detector's surroundings. The CCD is required to be capable of small movements in the X, Y, and Z directions. These aspects will greatly increase the difficulty of the thermal design. Based on the difficulty of the thermal design and the factors that influence the temperature of the CCD, large-thermal-resistance insulating technology is adopted and a detailed thermal design is performed [12]. Thermal simulation and a thermal balance test are then carried out to verify the correctness of the thermal design.

Received 29 November 2017; revision received 12 June 2018; accepted for publication 8 July 2018; published online 29 October 2018.

*Ph.D. Candidate, Thermal Control Group, Changchun Institute of Optics, Fine Mechanics and Physics; also University of Chinese Academy of Sciences, 100049 Beijing, People's Republic of China; lishijun15@mails.ucas.ac.cn.

†Professor, Thermal Control Group, Changchun Institute of Optics, Fine Mechanics and Physics; chenliheng3@163.com (Corresponding Author).

‡Master Degree Candidate, Thermal Control Group, Changchun Institute of Optics, Fine Mechanics and Physics; also University of Chinese Academy of Sciences, 100049 Beijing, People's Republic of China; wuyuhua16@mails.ucas.ac.cn.

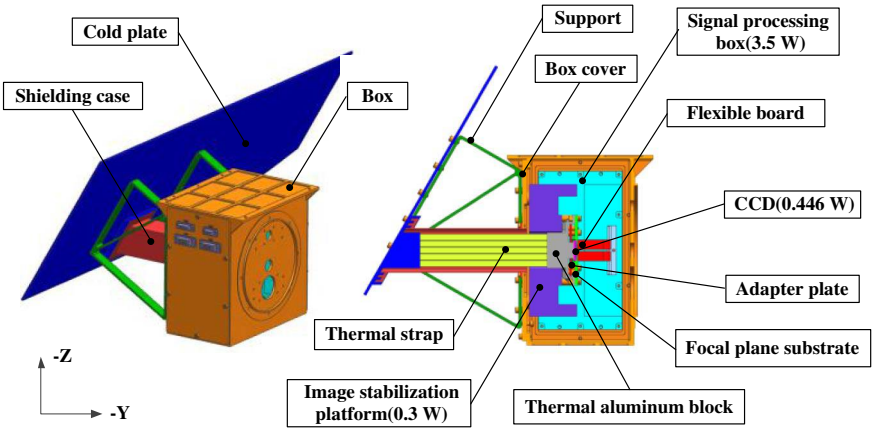

Fig. 1 Structure of detector.

II. Structure and Thermal Control Index of the Detector

A. Structure

The detector structure, as shown in Fig. 1, mainly includes the CCD, a focal plane substrate, an image stabilization platform, a thermal aluminum block, two thermal straps, a cold plate, and a signal processing box. Figure 1 shows that the CCD is fixed on the focal plane substrate, and the focal plane substrate is connected to the image stabilization platform; the image platform is then mounted on the box cover, and the cold plate is installed on the box cover by the supports. Additionally, the image stabilization platform is driven by a piezoelectric ceramic to allow the CCD to be moved in the X, Y, and Z directions. The detector is cooled using two flexible copper thermal straps that are connected to the radiant cold plate to ensure that it remains within the required operating temperature range. The heat sources for the detector (including the CCD, the image stabilization platform, and the signal processing box) are all in long-term operation; and the power consumptions of the CCD, the image stabilization platform, and the signal processing box are 0.446, 0.3, and 3.5 W, respectively, as shown in Fig. 1. The overall configuration of the XEUVI and the position of the detector are provided in the imager, as shown in Fig. 2. Meanwhile, the relative position of the XEUVI and the solar spectrometer that is around the imager are provided in the satellite platform, as shown in Fig. 3.

B. Thermal Control Index

Based on the performance requirements of the XEUVI, the thermal control indices of the focal plane assembly and the related components are explained, with the main components being the CCD and the image stabilization platform.

1) The temperature range for the CCD is −75 to −55°C.

2) The temperature range for the image stabilization platform is -5 ± 2°C.

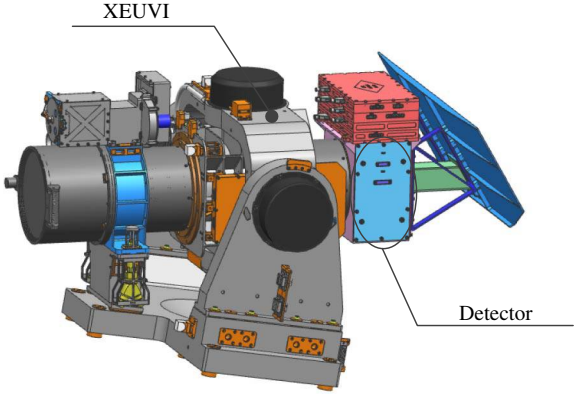

Fig. 2 Overall configuration of the XEUVI.

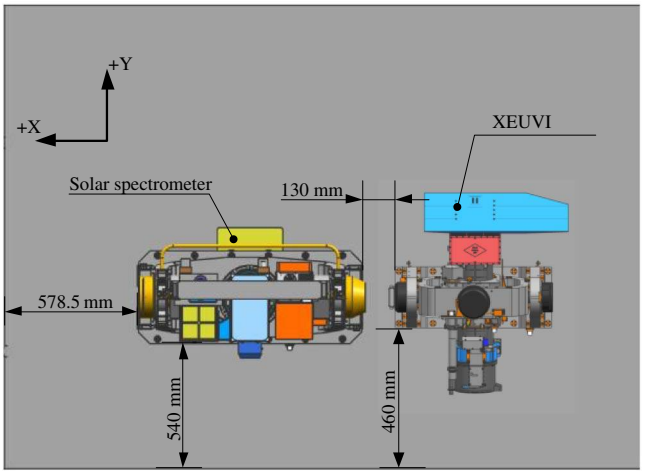

Fig. 3 Relative position of the XEUVI and the solar spectrometer.

III. External Heat Fluxes Analysis

The size and variation of the external heat fluxes are among the most important conditions for thermal design and are the basis of the thermal analysis calculations and the accurate simulations of the external heat fluxes during the thermal test [13]. Therefore, the external heat fluxes of the imager are analyzed first in the thermal design process. The imager works in a sun-synchronous orbit with a track height of 836 km and an orbit inclination of 98.76 deg, and the local time of the satellite through the ascending node is 18:00 ~ 18:20.

The imager's forward flight direction is defined as the $+X$ direction, whereas the direction toward the ground is defined as the $+Z$ direction and the $+Y$ direction is determined by the right-hand rule. Based on the imager's orbit type and parameters, its annual beta angle (β) can be obtained by Satellite Tool Kit software, with results as shown in Fig. 4. The maximum beta angle (β_{max}) and the minimum beta angle (β_{min}) are given in Table 1. The external heat fluxes for β_{max} and β_{min} are analyzed using the I-deas thermal model generator (TMG) thermal analysis software to obtain external heat fluxes for each surface (except for the imager installation surface) in a single orbital period, as shown in Figs. 5 and 6. The average external heat fluxes of the imager's surfaces for one orbital period are given in Table 2. The external heat fluxes in this part are arrival fluxes.

Because the mounting surface is on the $+Z$ surface, the external heat fluxes of the mounting surface are not taken into account in the design. The data above show that the $+Y$ surface is almost free from external heat fluxes all year round. The external heat fluxes of the $+X$ surface, the $-X$ surface, and the $-Z$ surface are all low and are related to β. The maximum average external heat fluxes of the $+X$ surface

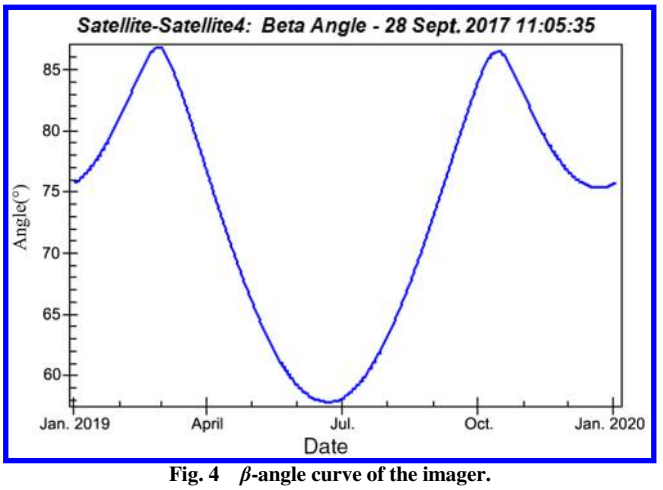

Fig. 4 β-angle curve of the imager.

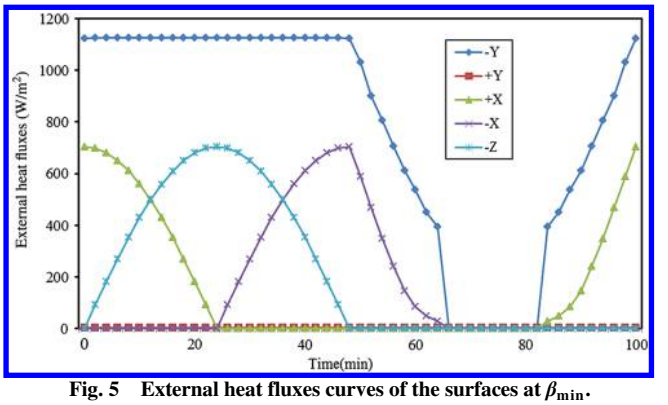

Fig. 5 External heat fluxes curves of the surfaces at β_{min}.

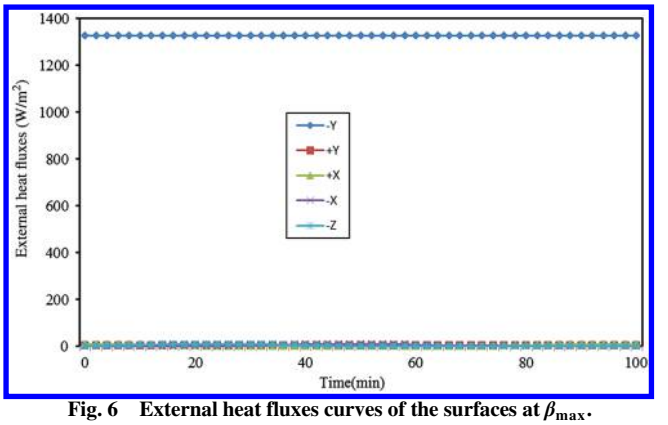

Fig. 6 External heat fluxes curves of the surfaces at β_{max}.

and the $-X$ surface are less than 160 W/m^2, and the $-Z$ surface is less than 210 W/m^2. Under the cover of the sun panel, the external heat fluxes of the $+X$ surface, the $-X$ surface, and the $-Z$ surface will be lower. Therefore, it is reasonable to define the $+Y$ surface as the heat dissipation surface.

IV. Thermal Design of Detector Components

A. Thermal Design Difficulty and Analysis of the Factors Affecting the CCD

The CCD is the most important component of the entire optical system [14], with its operating temperature range of −75 to −55°C and its high-precision requirements. The temperature of the tube and the optical components around the CCD is approximately 20°C, and there is a large temperature difference between the components and the CCD. Additionally, the CCD is fixed on the image stabilizer assembly, which is required to achieve small-scale movements in the X, Y, and Z directions. These factors pose considerable challenges for the thermal design. Therefore, it is necessary to adopt a specific thermal control measure for the thermal design that can not only ensure the thermal resistance of the heat transfer path to maintain the temperature within the required range but can also reduce the impact on the surrounding components to a minimum by thermal isolation.

Based on the relationships among the detector components, a diagram of the factors influencing the temperature of the CCD is shown in Fig. 7. The focal plane assembly of the CCD and the surrounding structures includes the focal plane substrate, the thermal aluminum block, the thermal straps, the radiation cold plate, the adapter plate, and the signal processing box. First of all, to reduce the radiation heat exchange among the components, radiation shielding measures are applied to the surfaces of the components, including a gold-plated finish, multilayer insulation (MLI), and aluminized tapes. After radiation shielding measures are taken, the influence of radiation on the CCD is very small. Therefore, the influence of the conduction among the components on the CCD is mainly analyzed in Fig. 7. The focal plane substrate, the adapter plate, and the thermal aluminum block are directly connected to the CCD and transfer heat to the CCD through conduction. The conduction relationships among the components are shown in Fig. 7.

By analyzing the thermal effects of each component on the CCD and considering the design difficulty, the thermal design of the detector is mainly based on adoption of thermal conduction measures (interfaces that are filled with thermally conductive filler), thermal insulation measures (heat insulation pads are adopted between interfaces), thermal dissipation measures (surfaces are sprayed with S781 white paint), and thermal compensation measures (patch heaters are used for temperature control).

B. Thermal Conduction Measures

To ensure that the temperature of the CCD is maintained at the required level and that the temperature is uniform, the heat generated by the power consumption of the CCD must be discharged in time. How to transfer the heat generated by the CCD to the heat dissipation surface located outside the device is an important issue in the thermal design of space-based optical remote sensors at present, under the premise that the heat transfer is guaranteed to not affect the focusing action. To control the CCD temperature within the −75 to −55°C range, a dedicated cooling channel is designed for the CCD that includes a thermal aluminum block, two thermal straps, and a cold plate. The specific thermal designs are as follows:

1) The interfaces between the CCD and the thermal aluminum block, the thermal aluminum block and the flexible copper thermal straps, and the thermal straps and the cold plate are all considered to be thermal installations, with interfaces that are filled with thermally conductive filler.

2) The interface between the signal handling box and the outer box is also considered to be a thermal installation.

C. Thermal Insulation Measures

As shown in Fig. 7, the CCD received three parts of heat:

Table 1 Times and angles of β_{max} and β_{min}

Name	Date/time	Angle, deg
β_{min}	21 June 2019/14:17	57.8
β_{max}	27 Feb. 2019/10:04	87.0

Table 2 Average external heat fluxes for each imager surface (units of watts per square meter)

Name	$-Y$	$+Y$	$+X$	$-X$	$-Z$
β_{min}	773.1	3.1	159.0	145.7	203.0
β_{max}	1328.2	2.9	3.6	3.3	3.2

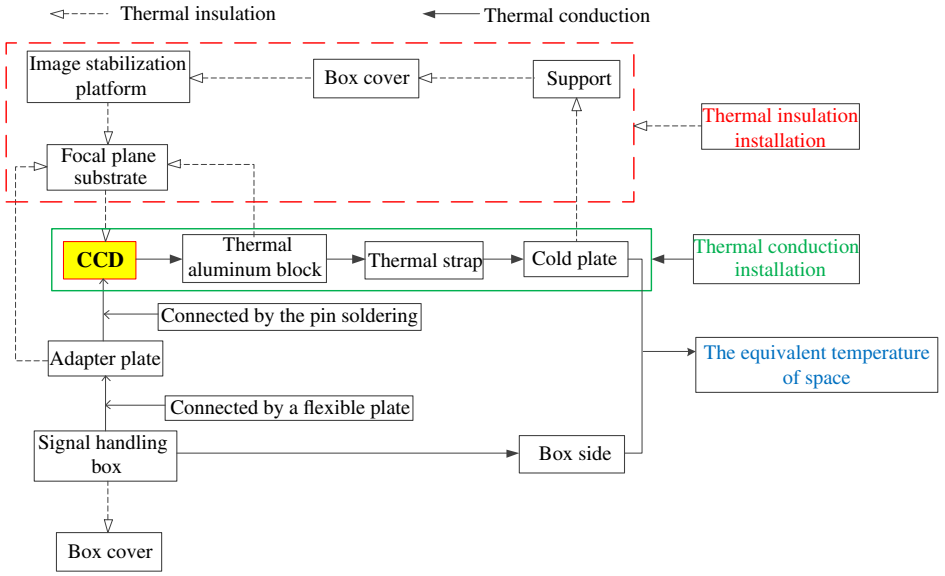

Fig. 7 Diagram showing factors influencing the temperature of the CCD.

1) Heat from the box cover is transferred to the CCD through the image platform and the focal plane substrate in turn.

2) Heat from the signal processing box is also transferred to the CCD through the flexible board and the adapter plate in turn.

3) The CCD will be subject to radiation heat transfer from components including the image stabilization platform, the signal processing box, the thermal straps, the thermal aluminum block, and the box.

To reduce the heat transferred to the CCD, a thermal insulation design based on large thermal resistance is used in the conductive paths between the components, and the surfaces of components that are capable of radiation heat transfer are coated with MLI or low-emission coatings. The thermal insulation design aspects based on large thermal resistance are as follows:

1) A thermal insulation installation is used between the image stabilization platform and the box cover, with four titanium alloy gaskets and four titanium alloy screws.

2) A thermal insulation measure is applied between the focal plane substrate and the image stabilization platform, with eight polyimide insulation mats and eight titanium alloy screws.

3) A thermal insulation installation using a small plane is applied between the CCD and the focal plane of the substrate, whereas the CCD is mounted on the adapter plate by pin soldering. In addition, another thermal insulation installation is adopted between the adapter plate and the focal plane of the substrate.

4) The thermal aluminum block and the focal plane substrate are connected using a small plane with two titanium-alloy flexible fixing assemblies.

5) The cold plate is installed on the box cover through the cold-plate supports. A thermal insulation installation is also used between the cold plate and its supports, with ten polyimide insulation mats and ten titanium alloy screws; and another thermal insulation installation is used between the support and the box cover.

The main aspects of the radiation insulation design are as follows:

1) The inner surface of the box is covered with three units of MLI.

2) The surfaces of the image stabilization platform, the thermal straps, and the signal handling box (except for the installation surfaces) are also covered with three units of MLI.

3) The surfaces of the focal plane substrate and the thermal aluminum block are gold plated to reduce their surface emissivity for radiation shielding purposes.

D. Thermal Dissipation Measures

To reduce the effects of the signal processing box on the other components, a 120×260 mm cooling surface that is sprayed with S781 white paint is opened on the side of the box on which the signal processing box is installed. In addition, to adapt to the constantly changing orientation of the tube in orbit and to minimize the effects of the solar panel and the cooling face of the platform on the cold plate, a great deal of optimization work is performed on the inclination, the area, and the dimensions of the cold plate. The final optimization results show that the angle between the solar panel and the cooling face of that platform that has the lowest impact on the cold plate is 30 deg. The cold-plate area is 203,391 mm^2, where the $+Y$ surface is sprayed with S781 white paint and the $-Y$ surface is covered with MLI, as shown in Fig. 8.

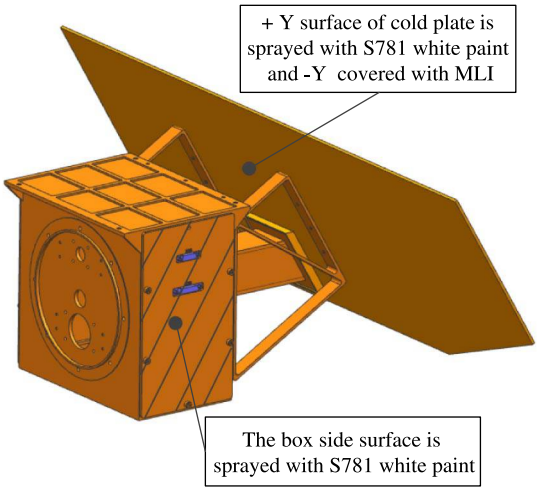

Fig. 8 Thermal design of the heat dissipation surface.

E. Thermal Compensation Measures

To prevent the temperature of the CCD from becoming too low, a heating zone is set on the thermal aluminum block for temperature compensation. In addition, to control and maintain the temperature of the image stabilization platform at -5°C, a heating zone is also provided on the image stabilization platform that uses temperature sensors to control the temperature with a closed-loop system.

V. Thermal Analysis

A. Establishment of Thermal Analysis Mode

When the thermal analysis model is established, the use of larger numbers of meshes is not necessarily best [15,16]. On the contrary,

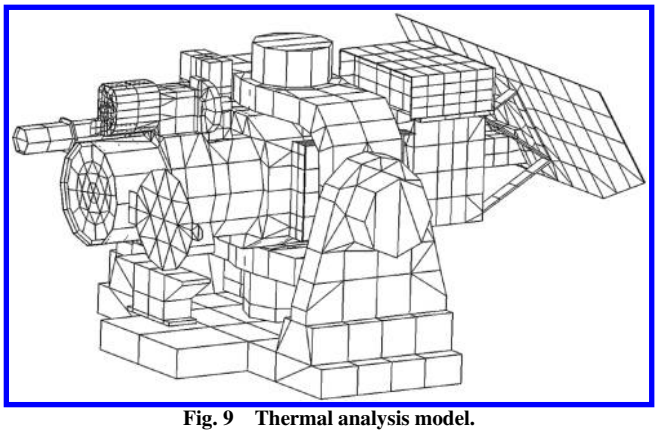

Fig. 9 Thermal analysis model.

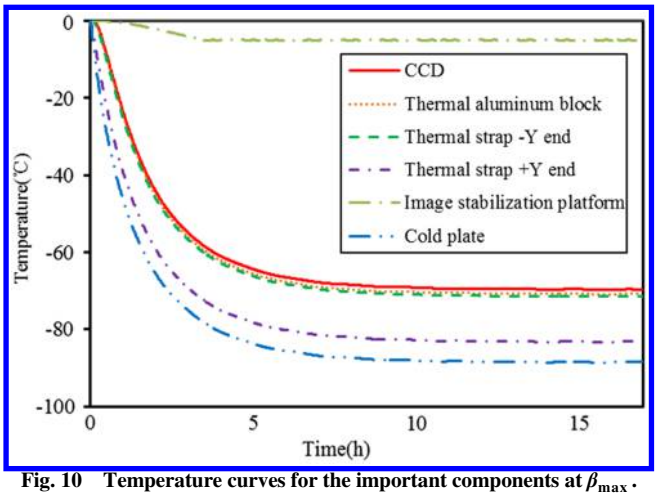

Fig. 10 Temperature curves for the important components at β_{max}.

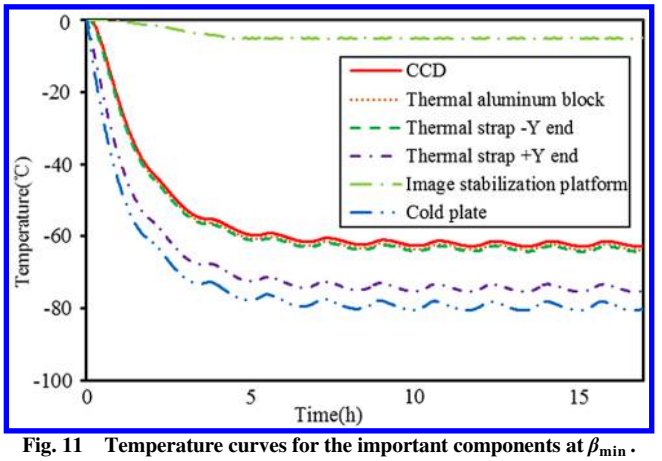

Fig. 11 Temperature curves for the important components at β_{min}.

meshes that are divided too small will reduce the efficiency of the thermal analysis. Therefore, without affecting the heat transfer path, the model should be simplified by setting as many thermal couplings as possible.

A finite element model for the thermal analysis is established using TMG software, as shown in Fig. 9. The thin-walled components in the XEUVI are simplified through use of shell elements, and the thicknesses of these elements are calculated based on the volume equivalent thickness. The model is divided into 8650 elements. During modeling, the thermal coupling method is used to simplify the process. A total of 126 thermal couplings is established within the thermal analysis model. The optical components are modeled using solid elements.

B. Definition of Thermal Analysis Conditions

The XEUVI works on a long-term basis over the entire orbit period. The thermal analysis conditions are therefore determined based on the results of the external heat fluxes analysis and the working modes of the imager. Different extreme conditions are defined under different β angles [17]. The dates that correspond to the different β angles are then determined. According to the specific dates, when the β_{max} is 87 deg, the solar constant is 1412 W/m^2. Similarly, when the β_{min} is 57.8 deg, the solar constant is 1322 W/m^2. At the same time, based on the different β angles, corresponding adjustments are made to the angle of the imager tube. The contact thermal conductivity is 2.51×10^{-4} $W/m/K$ between the MLI and the component, and the unit number of the MLI is 20. The MLI surface is polytetrafluoroethylene film (F46), with performance parameters of $\alpha_s/\varepsilon = 0.16/0.69$ for the beginning of life and $\alpha_s/\varepsilon = 0.36/0.69$ for the end of life. The heat dissipation surface is sprayed with S781 white paint, with the performance parameters of $\alpha_s/\varepsilon = 0.17/0.87$ for the beginning of life and $\alpha_s/\varepsilon = 0.35/0.87$ for the end of life. The heat sources are in long-term operation, and the active thermal control process works. The imager is installed on the satellite platform with a temperature range of -20 to 45°C. In addition, the thermal interface temperature of the detector is 10°C.

C. Calculation Results for the Thermal Analysis

Based on the thermal control measures and the conditions defined previously, the transient thermal analysis is carried out. The temperature curves for the important components of the imager are shown in Figs. 10 and 11.

The temperature data of the key components are sorted based on the results of the thermal analysis, as shown in Table 3, which includes the temperature ranges of the CCD, the image stabilization platform, the thermal aluminum block, both ends of the thermal strap, and the cold plate.

Because the orbit at β_{max} has the full sunshine area, Fig. 8 indicates that the temperatures of the important components show almost no fluctuations. However, the orbit at β_{min} has a shadow area of 16.2 min, and so the temperatures of the key components will show some fluctuations, as illustrated in Fig. 11. Despite these fluctuations, the temperatures of the components all remain within the required range. Table 3 shows that the CCD's temperature for the two extreme conditions ranges from -69.7 to -61.3°C. Under two conditions, although the temperature of the image stabilization platform can be controlled at -5°C, the actual heating power consumption figures are different. The power consumption of the image stabilization platform heating zone is 2.33 W at β_{max} and 2.12 W at β_{min}. The components all meet their thermal design requirements, and the thermal design is thus both effective and feasible.

VI. Thermal Balance Test

At present, because the thermal design cannot rely on solely on analyses and calculations to solve the thermal design problems, sufficient ground simulation tests must also be carried out to verify

Table 3 Temperature data of the important components at different β angles (units of degrees Celsius)

Conditions	CCD	Image stabilization platform	Thermal aluminum block	Thermal strap $-Y$ end	Thermal strap $+Y$ end	Cold plate
β_{max}	$-69.7 \sim -69.5$	$-5.1 \sim -4.9$	$-70.8 \sim -70.7$	$-71.5 \sim -71.3$	$-83.3 \sim -83.1$	$-88.6 \sim -88.4$
β_{min}	$-62.8 \sim -61.3$	$-5.1 \sim -4.9$	$-63.8 \sim -62.3$	$-64.3 \sim -62.8$	$-75.5 \sim -73.3$	$-80.7 \sim -78.1$

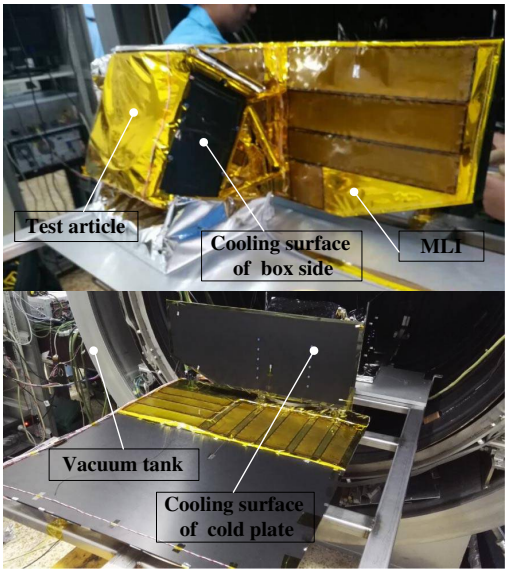

Fig. 12 Physical map of the thermal balance test scheme.

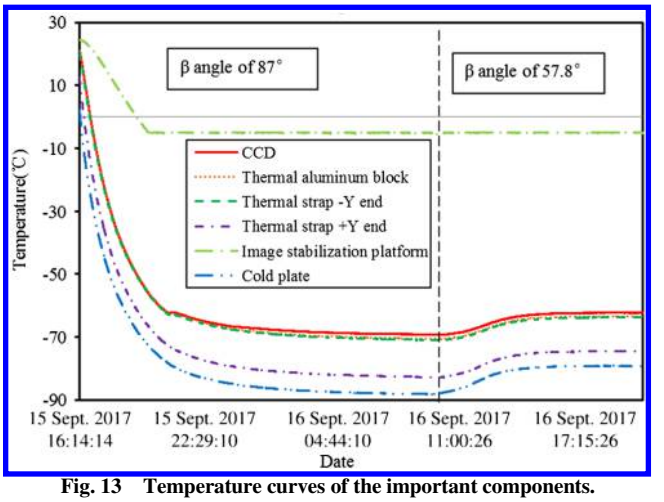

Fig. 13 Temperature curves of the important components.

the correctness of the thermal design. The thermal balance test is a supplement and verification for the thermal analysis. The results of the thermal balance test are the temperature data of the XEUVI that would be produced under actual operating conditions. Using the test data, the thermal analysis model can be modified, and further guidance can be provided for design optimization.

A. Test Scheme

In the thermal balance test of the detector, a vacuum tank is used to simulate the space environment, and the absorbed external heat fluxes is simulated using a heater. A physical map of the thermal balance test scheme is shown in Fig. 12, and it includes the test article, the components for simulation of the boundary conditions, and the vacuum tank.

B. External Heat Fluxes Simulation

1. *External Heat Fluxes Simulation of MLI Surfaces*

Onorbit external heat fluxes are obtained by calculation. According to the actual areas of the surfaces, the external heat fluxes' data of the test are obtained. Then, the experimental working currents of the simulated external heat flux heater are calculated. The simulation of the heating circuit currents is adjusted to make external heat fluxes of the MLI surfaces agree with the orbital period average data.

2. *External Heat Fluxes Simulation of Cooling Surfaces*

The external heat fluxes of the cooling surfaces are obtained by the thermal analysis calculation. Then, the external heat fluxes' data of the test are obtained. According to the actual state of the product, the heating sheet is used to simulate the absorbed heat of the cooling surfaces.

It can be seen from Table 4 that the test values of the power consumption are basically the same as the design values of the power consumption, and the test values are slightly larger than the design values, which indicate that the test values are reasonable and effective.

C. Test Results and Analysis

The thermal balance test conditions are divided into $\beta_{\max}$ and $\beta_{\min}$ to correspond to the working modes of the thermal analysis, and the temperature curves for the most important components are shown in Fig. 13. During the test process, the vacuum is the 1.2×10^{-5} Pa to 9.9×10^{-5} Pa range, and the temperature of the heat sink is 100 K. In addition, the temperature at the box installation boundary is 10.1°C, and the temperature at the tube installation boundary is 20.1°C.

Based on the results of the thermal tests, the temperature data for the important components are listed as shown in Table 5, and they include the temperatures of the CCD, the image stabilization platform, the thermal aluminum block, both ends of the thermal strap, and the cold plate.

The test data in Table 5 show that the temperature of the CCD ranges from −69.3 to −62.2°C, and that the temperature of the image stabilization platform can be controlled to remain at −5°C, meeting the thermal control index requirements. Additionally, the temperature distributions of the other important components are correct, and the accuracy of the thermal design is thus verified. Although the temperature of the image stabilization platform can be controlled at −5°C, the actual heating power consumption figures are different. The power consumption of the image stabilization platform heating zone is 2.45 W at $\beta_{\max}$ and 2.27 W at $\beta_{\min}$.

Table 4 External heat fluxes simulation on the thermal key parts

Position	Size of heating sheet, mm × mm	Number	Heat power of $\beta_{\max}$		Heat power of $\beta_{\min}$	
			Design value, W^{-1}	Test value, W^{-1}	Design value, W^{-1}	Test value, W^{-1}
Cooling surface of box	80 × 90	1	0.37	0.39	1.04	1.08
MLI of cold plate	60 × 260	2	28.46	28.55	18.68	18.73
	75 × 160	2				
	70 × 300	2				
	60 × 300	1				
Cooling surface of cold plate	60 × 260	2	3.54	3.62	2.76	2.82
	75 × 160	2				
	70 × 300	2				
	60 × 300	1				
	80 × 90	1				

Table 5 Temperature data of the most important components from the thermal balance test (units of degrees Celsius)

Conditions	CCD	Image stabilization platform	Thermal aluminum block	Thermal strap $-Y$ end	Thermal strap $+Y$ end	Cold plate
β_{max}	$-69.3 \sim -69.2$	$-5.1 \sim -4.9$	$-70.5 \sim -70.4$	$-70.9 \sim -70.8$	$-82.6 \sim -82.5$	$-88.2 \sim -88.1$
β_{min}	$-62.3 \sim -62.2$	$-5.1 \sim -4.9$	$-63.5 \sim -63.4$	$-63.8 \sim -63.7$	$-74.6 \sim -74.5$	$-79.2 \sim -79.1$

The simulated external heat fluxes data are calculated based on the input conditions provided by the satellite system. The results are also checked by other thermal control staff using different software. The temperature data at the test boundaries are derived from the relevant analyses and the design report with high reliability.

VII. Conclusions

In this paper, according to the space environment and the structural characteristics and working modes of the detector, a detailed thermal design of the detector was carried out using a combination of passive and active thermal controls. Given the difficulty of the thermal design of the detector, and the factors influencing the temperature of the CCD, large-thermal-resistance technology was proposed. Eventually, the thermal design problem was successfully solved. The results of the thermal analysis showed that the temperature of the CCD ranged from -69.7 to -69.5°C at β_{max}, whereas this temperature ranged from -62.8 to -61.3°C at β_{min}. The ranges met the thermal control index requirements well and verified the effectiveness of the proposed thermal design. During the thermal balance test process, the CCD temperature was from -69.3 to -69.2°C at β_{max} and -62.3 to -62.2°C at β_{min}. The test values were in good agreement with the results of the thermal analysis. Additionally, the results of the thermal balance test met the thermal design requirements, and thus verified that the proposed thermal design was correct.

Acknowledgment

The work is supported by Major Projects of China and Youth Innovation Promotion Association of the Chinese Academy of Science under grant no. 2015173.

References

[1] Li, B. Q., Zhu, G. W., Wang, S. J., Lin, H. A., Peng, J. L., and Liu, J., "The Solar X-EUV Imaging Telescope," *Chinese Journal of Geophysics*, Vol. 48, No. 2, 2005, pp. 235–242. doi:10.3321/j.issn:0001-5733.2005.02.001

[2] Peng, J. L., Zhu, G. W., Wei, F., and Li, B. Q., "Solar Extreme Ultraviolet Multichannel Imager," *Chinese Journal of Space Science*, Vol. 29, No. 4, 2009, pp. 417–421. doi:10.11728/cjss2009.04.417

[3] Morris, S., "The Pioneer Spacecraft," *American Journal of Physics*, Vol. 74, No. 5, 2006, pp. 373–373. doi:10.1119/1.2167765

[4] Noci, G., "The Solar and Heliospheric Observatory," *International Astronomical Union Colloquium*, Vol. 86, 1984, pp.155–158. doi:10.1017/S0252921100085596

[5] Ichimoto, K., Tsuneta, S., Suematsu, Y., Shimizu, T., Otsubo, M., and Kato, Y., "The Solar Optical Telescope Onboard the Solar-B," *Proceedings of the Society of Photo-Optical Instrumentation Engineers*, Vol. 5478, 2004, pp. 1142–1151. doi:10.1117/12.550989

[6] Sakao, T., Kano, R., Hara, H., Matsuzaki, K., Shimojo, M., and Tsuneta, S., "Focal Plane CCD Camera for the X-Ray Telescope (XRT) Aboard SOLAR-B," *Proceedings of the Society of Photo-Optical Instrumentation Engineers*, Vol. 5487, 2004, pp. 1189–1198. doi:10.1117/12.551742

[7] Seely, J. F., Windt, D., Donguy, S., Brown, C., Hlland, G., and Hunter, W., "Performance of Multilayer-Coated Gratings for the Extreme-Ultraviolet Imaging Spectrometer (EIS) for the Solar-B Mission," *Proceedings of the Society of Photo-Optical Instrumentation Engineers*, Vol. 5168, 2004, pp. 12–20. doi:10.1117/12.507160

[8] Barraclough, S., Merrill, O., and Damasio, C., "Solar Orbiter Thermal Design and Verification Approach," *AIAA 41st International Conference on Environment Systems*, AIAA Paper 2011-5192, 2011. doi:10.2514/6.2011-5192

[9] Müller, D., "Solar Orbiter," *Solar Physics*, Vol. 285, No. 1, 2013, pp. 25–70. doi:10.1007/s11207-012-0085-7

[10] Pérez, J. M. S., "Solar Orbiter Mission Design Overview and Navigation Analysis," *AIAA/AAS Astrodynamics Specialist Conference*, AIAA Paper 2016-5668, 2016. doi:10.2514/6.2016-5668

[11] Huang, G., Zhang, H., and Yang, J., "Thermal Design and Analysis of a Hard X-Ray Modulation Telescope," *Journal of Thermophysics and Heat Transfer*, Vol. 22, No. 3, 2008, pp. 528–530. doi:10.2514/1.34467

[12] Totani, T., Ogawa, H., Inoue, R., Das, T. K., Wakita, M., and Nagata, H., "Thermal Design Procedure for Micro- and Nanosatellites Pointing to Earth," *Journal of Thermophysics and Heat Transfer*, Vol. 28, No. 3, 2014, pp. 524–533. doi:10.2514/1.T4306

[13] Zi, K. M., Wu, Q. W., Li, Z., and Liu, X., "Simulation Analysis of a Space Optical Remote Sensor's Thermal Design," *Computer Simulation*, Vol. 25, No. 12, 2008, pp. 77–80. doi:10.3969/j.issn.1006-9348.2008.12.021

[14] Guo, L., Zhang, X. S., Huang, Y., Hu, R. C., and Liu, C. L., "Thermal Characterization of a New Differential Thermal Expansion Heat Switch for Space Optical Remote Sensor," *Applied Thermal Engineering*, Vol. 113, Nov. 2017, pp. 1242–1249. doi:10.1016/j.applthermaleng.2016.11.102

[15] Luo, J. F., Yi, H. L., Tan, H. P., and Yang, L.-J., "Thermal Analysis of Optical Windows for Spacecraft Applications," *Journal of Thermophysics and Heat Transfer*, Vol. 22, No. 2, 2008, pp. 296–301. doi:10.2514/1.27856

[16] Caldwell, N., Gutmark, E., and Ruggeri, R., "Thermal Analysis of a Blade-Twist Actuator System," *Journal of Thermophysics and Heat Transfer*, Vol. 21, No. 4, 2007, pp. 712–719. doi:10.2514/1.30022

[17] Mitchao, D. P., Totani, T., Wakita, M., and Nagata, H., "Preliminary Thermal Design for Microsatellites Deployed from International Space Station's Kibo Module," *Journal of Thermophysics and Heat Transfer*, Vol. 32, No. 3, 2018, pp. 1–10. doi:10.2514/1.T5367